ACSNANO

www.acsnano.org

# Two-Dimensional Nonvolatile Valley Spin Valve

Kai Huang, Kartik Samanta, Ding-Fu Shao, and Evgeny Y. Tsymbal*

Cite This: *ACS Nano* 2025, 19, 3448−3454

Read Online

ACCESS | Metrics & More | Article Recommendations | Supporting Information

**ABSTRACT:** **A spin valve represents a well-established device concept in magnetic memory technologies, whose functionality is determined by electron transmission, controlled by the relative alignment of magnetic moments of the two ferromagnetic layers. Recently, the advent of valleytronics has conceptualized a valley spin valve (VSV)—a device that utilizes the valley degree of freedom and spin-valley locking to achieve a similar valve effect without relying on magnetism. In this study, we propose a nonvolatile VSV (*n*-VSV) based on a two-dimensional (2D) ferroelectric semiconductor where resistance of *n*-VSV is controlled by a ferroelectric domain wall between two uniformly polarized domains. Focusing on the 1T″ phase of $MoS_2$, which is known to be ferroelectric down to a monolayer and using density functional theory combined with quantum transport calculations, we demonstrate that switching between the uniformly polarized state and the state with oppositely polarized domains separated by a domain wall results in a resistance change of as high as $10^7$. This giant VSV effect occurs due to transmission being strongly dependent on matching (mismatching) the valley-dependent spin polarization in the two domains with the same (opposite) ferroelectric polarization orientations, when the chemical potential of 1T″-$MoS_2$ lies within the spin-split valleys. The proposed *n*-VSV can be employed as a functional device for high-performance nonvolatile valleytronics.**

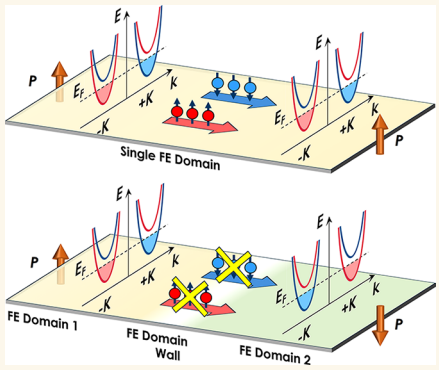


**KEYWORDS:** *valleytronics, valley spin valve, ferroelectricity, domain wall, 2D van der Waals material, nonvolatile*

## INTRODUCTION

A spin valve is a spintronic device widely used for information technologies.[1−4] It typically consists of two ferromagnetic layers separated by a thin nonmagnetic spacer layer, either metallic or insulating, in the latter case being known as a magnetic tunnel junction. The functional property of a spin valve is a change between high and low transmission states, depending on whether the magnetization directions of the two magnetic layers are parallel or antiparallel. In the parallel state, the spin configurations of the magnetic electrodes align, leading to high transmission, while in the antiparallel state, their misalignment leads to low transmission.[5,6] This results in a giant (tunneling) magnetoresistance effect useful for information readout in modern hard drive read heads and magnetic random access memories.[7,8]

Recently, with the advancement of two-dimensional (2D) van der Waals (vdW) materials, the concept of a valley spin valve (VSV) has emerged.[9−11] This idea utilizes a valley degree of freedom to modulate the spin configuration at the Fermi surface and create a spin valve. Valleys are separated energy extrema in the electronic band structure in the momentum space.[12−21] In a nonmagnetic material with space inversion ($\hat{P}$) and time reversal ($\hat{T}$) symmetries, the valleys at nontime-reversal-invariant momenta (non-TRIMs), $+K$ and $-K$, are spin degenerate due to a combined $\hat{P}\hat{T}$ symmetry. Application of an external electric field $E$ breaks $\hat{P}$ symmetry, leading to spin splitting with opposite spin polarizations at valleys $+K$ and $-K$ due to $\hat{T}$ symmetry. Changing the sign of $E$ is equivalent to the $\hat{P}$-symmetry operation, under which the momentum $+K$ transforms to $-K$, while the spin remains invariant. The valley-dependent spin polarization is thus fully reversed by an electric field of opposite sign. This property makes valley materials useful to build a VSV. Using two independent gates to control the spin polarization of the valleys in the two separated regions of the valley material under the applied electric fields allows control of transmission across the gates. The transmission of the VSV is high or low, depending on the electric fields at the gates pointing in the same or opposite directions, respectively. So far, 2D materials, such as stanine, germanene,[10] and $(Pt/Pd)_2HgSe_3$,[11] have been predicted to develop a valley spin polarization under an applied electric field and thus to be able

Received: September 12, 2024
Revised: December 27, 2024
Accepted: December 31, 2024
Published: January 13, 2025

ACS Publications © 2025 American Chemical Society



https://doi.org/10.1021/acsnano.4c12812
*ACS Nano* 2025, 19, 3448−3454

Downloaded from pubs.acs.org/ancac3/article-pdf/19/3/3448/4225429/nn4c12812.pdf by WESTLAKE UNIV. Yudi Yang on 17 October 2026

to constitute a VSV. In addition to memory elements, VSVs can serve as logic gates that satisfy the concatenation requirement, where the output voltage of the logic gate can be used as an input of a successive gate.[22]

While the proposed concept of a VSV is interesting from the fundamental point of view and useful for practical applications, it suffers from the inability of nonvolatile performance. Nonvolatile memories, as opposed to volatile, allow retaining data even when not powered. The proposed VSV, however, requires an external electric field to retain the data and thus is volatile. It would be desirable from the practical perspective to develop a concept of a nonvolatile VSV ($n$-VSV) which can potentially serve as the key element of low-power nonvolatile memories and logic.[23] At the same time, from the fundamental science perspective, new knowledge about the properties of 2D ferroic materials exhibiting valley spin polarization is required to develop an $n$-VSV.

2D vdW ferroelectrics with their spontaneous electric polarization are good candidates to realize an $n$-VSV. Since the polarization naturally breaks $\hat{P}$ symmetry, a finite spin splitting is expected at valleys $+K$ and $-K$ even in the absence of an electric field (Figure 1a). If such a 2D ferroelectric is in a single domain state (i.e., polarization $P$ is uniform across the structure) and the Fermi level lies within the valleys, the spin states at each valley ($+K$ or $-K$) match along the transport direction and electron transmission is high (Figure 1a). On the contrary, if a 2D ferroelectric has two domains with antiparallel polarization $P\uparrow$ and $P\downarrow$, the spin states at each valleys mismatch along the transport direction across the two domains, leading to a low transmission (Figure 1b).

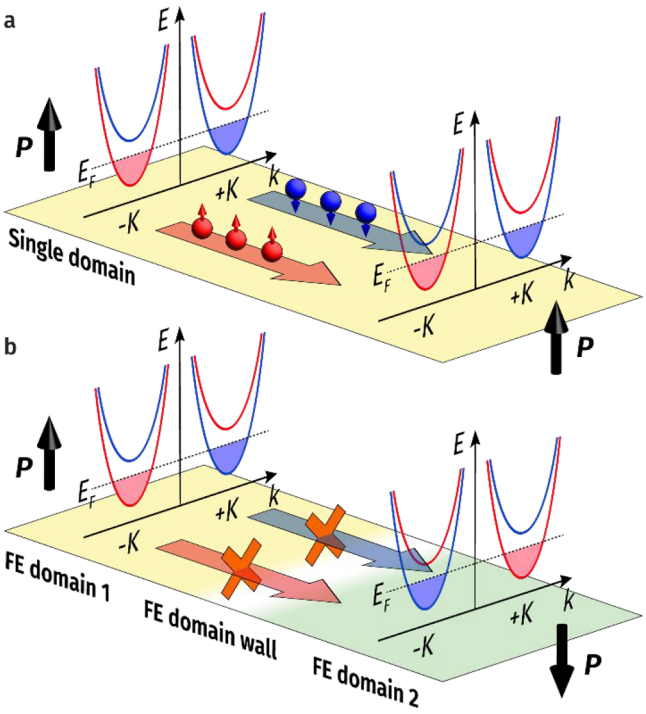


**Figure 1. Schematic of $n$-VSV based on a 2D ferroelectric material. (a) Spin-split band structures near $\pm K$ valleys for a single domain ferroelectric ($P\uparrow$). At each valley ($+K$ or $-K$), spin states at the Fermi energy ($E_F$) match along the transport direction, and electron transmission is high. Electrons with spin-up (down) are denoted by red (blue). (b) Spin-split band structures near $\pm K$ valleys for a ferroelectric representing two opposite ferroelectric domains ($P\uparrow$ and $P\downarrow$) separated by a domain wall. At each valley ($+K$ or $-K$), spin states at $E_F$ mismatch along the transport direction, and electron transmission is low.**

Among the 2D materials, 1H or 2H $MoS_2$ are widely used to investigate valley-dependent effects.[24−27] However, their point-group symmetries are inconsistent with the ferroelectricity. The same is true for 1T or 1T′ phases of $MoS_2$.[28,29] Recently, a ferroelectric 1T″ phase has been confirmed experimentally to occur in $MoS_2$ grown under appropriate conditions.[30−34] The 1T″ phase preserves ferroelectricity down to a monolayer limit and hosts valleys at $\pm K$ points.[31,32] These properties make 1T″ $MoS_2$ a good candidate to realize an $n$-VSV.

In this work, based on density functional theory (DFT) and quantum transport calculations, we predict that switching of monolayer 1T″ $MoS_2$ between the uniformly polarized state (UP state) and the state of two domains with opposite polarization separated by a domain wall (DW state) results in a giant change of transmission up to a factor of $10^7$. We show that the effect arises due to the valley spin polarization in monolayer 1T″ $MoS_2$ changing sign with reversal of electric polarization leading to spin mismatch when the UP state is flipped to the DW state.

## RESULTS

**Monolayer 1T″ $MoS_2$.** 1T″ phase $MoS_2$ is a distorted variant of the centrosymmetric 2D 1T phase $MoS_2$.[35−39] In its undistorted form, 1T $MoS_2$ consists of a trilayer structure with a molybdenum (Mo) atom surrounded by an octahedron of six sulfur (S) atoms. This undistorted 1T phase $MoS_2$ is highly unstable as a monolayer[40] and typically transforms into other more stable phases.[41−44] Among these, the 1T″ $MoS_2$[30,34,45−48] which exhibits both ferroelectricity and valleys at non-TRIM points,[31] is particularly suitable for an $n$-VSV.

The unit cell of 1T″ $MoS_2$ contains 4 Mo atoms and 8 S atoms and belongs to the polar space group $P3m1$, indicating its ferroelectric nature. The cell is $2 \times 2$ times as large as the centrosymmetric 1T phase unit cell due to the Mo atoms forming trimers (Figure 2a,b). In the $P\uparrow$ state, as shown in Figure 2a, the green Mo trimer has longer Mo−Mo distances, while the orange trimer has shorter distances. This distortion pulls the green S atom closer to the middle Mo plane and pushes the orange S atom away. Other S atoms are also affected, resulting in overall S anion movement in the $-z$ direction and polarization in the $+z$ direction ($P\uparrow$). In the $P\downarrow$ state, it can be achieved by the $\hat{P}$ operation of $P\uparrow$, and these movements are reversed, leading to polarization in the $-z$ direction.

Our DFT calculations, as detailed in Methods, confirm the structure and polarization properties of 1T″ $MoS_2$. The polarization (dipole moment per area) of the 2D material is calculated to be 0.25 pC/m along $z$-axis, aligning closely the value 0.24 pC/m obtained in previous studies.[34] The polarization is also confirmed by the nonzero $z$ displacement of the centers of positive and negative ions, $\overline{d}_z^{S}-\overline{d}_z^{Mo} = -0.0052$ Å for the $P\uparrow$ state, where $\overline{d}_z^{S}$ is the averaged $z$ displacement of 8 S atoms and $\overline{d}_z^{Mo}$ is the averaged $z$ displacement of 4 Mo atoms in the unit cell. Calculations based on the nudged elastic band (NEB) method[49] indicate that the polarization switching barrier of 1T″ $MoS_2$ is 66 meV per unit cell (Figure S1b).

Figure 2c,d shows the band structure of 1T″ $MoS_2$ in $P\uparrow$ and $P\downarrow$ states calculated with inclusion of SOC. The material exhibits a band gap of 0.14 eV, consistent with previously reported values ranging from 0.1 to 0.19 eV.[30,31,45] We find

Downloaded from pubs.acs.org/ancac3/article-pdf/19/3/3448/42225429/nn4c12812.pdf by WESTLAKE UNIV. Yudi Yang on 17 October 2026


https://doi.org/10.1021/acsnano.4c12812
ACS Nano 2025, 19, 3448−3454

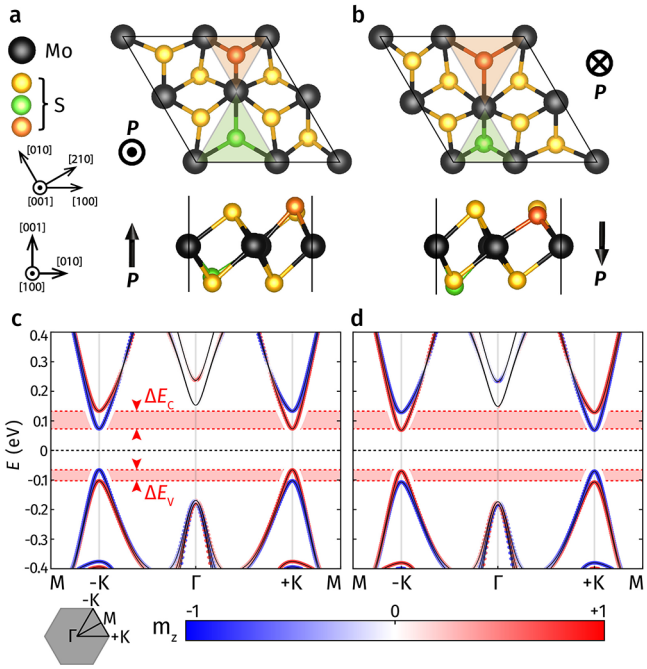


**Figure 2. (a, b) Structure of 1T″ $MoS_2$ unit cell in the top view (top) and side view (bottom) for the $P\uparrow$ state (a) and $P\downarrow$ state (b). Orange and green triangles denote Mo trimers. (c, d) Band structures for $P\uparrow$ state (c) and $P\downarrow$ state (d) 1T″ $MoS_2$. Spin projection to the direction of magnetization $m_z$ is shown in color. Horizontal dashed line indicates the Fermi energy ($E_F$). Hexagonal Brillouin zone and high symmetry points are shown at the bottom left.**

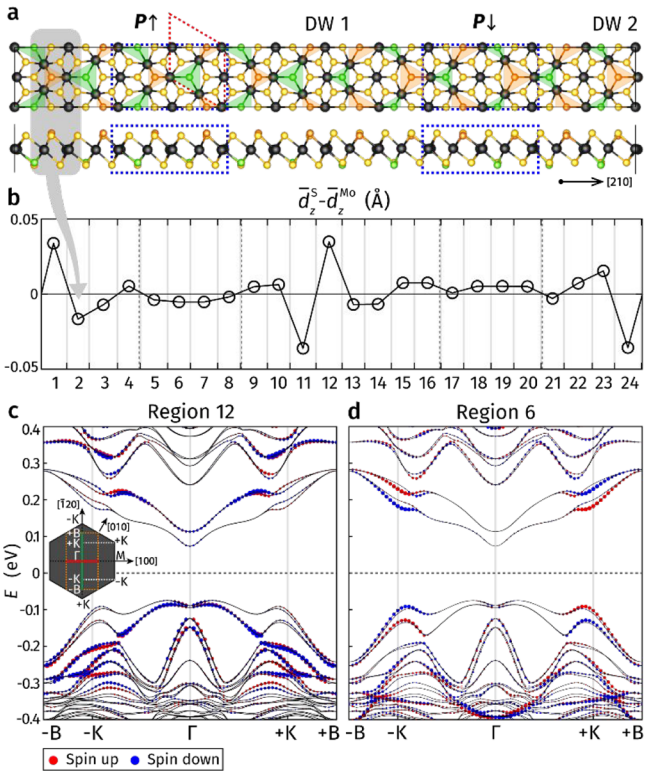


**Figure 3. (a) Top view (top) and side view (bottom) of the structure with DW separating $P\uparrow$ and $P\downarrow$ domains of 1T″ $MoS_2$. Atoms within the blue boxes represent fixed pristine domains, while other atoms are subjected to structural relaxation. Red dashed rhombus indicates the unit cell of the $P\uparrow$ domain. Orange and green triangles denote Mo trimers. (b) $\bar{d}_z^S$–$\bar{d}_z^{Mo}$ value for atoms in different regions in the structure of structurally relaxed DWs, as region 2 shown in gray as an example, numbered from 1 to 24, in the supercell structure. (c, d) Band structures (black lines) of the domain wall structure of 1T″ $MoS_2$. Spin projection to the direction of magnetization $m_z$ is shown in color. Width of the fat band represents the electron contribution from the atoms in regions 12 (c), 6 (d). Insert: Brillouin zone of the 1T″ $MoS_2$ hexagonal unit cell (dark gray), orthogonal super cell (orange), and the DW structure along [100] (green) and [$\bar{1}$20] (red). Here, directions are in reciprocal coordinates according to the hexagonal unit cell.**

valleys of the conduction band minimum (CBM) and valence band maximum (VBM) at the $\pm K$ points, where the Zeeman-like spin splitting for spin-up and spin-down electrons is induced by $\hat{P}$ symmetry breaking. The spin splitting is 60 meV for the valleys above the Fermi level and 37 meV for the valleys below it. We denote the energy windows for the valley-dependent spin splitting as $\Delta E_C$ and $\Delta E_V$ for the CBM and VBM, respectively. Due to $\hat{T}$ symmetry, the spin splittings at the $+K$ and $-K$ points are opposite. The valley-dependent spin polarizations of the $P\uparrow$ and $P\downarrow$ states are also opposite, as they are related by the $\hat{P}$ symmetry.

**Atomic and Band Structure of *n*-VSV.** An *n*-VSV requires switching between the UP and DW states. To model this, we combine the orthorhombic supercells of $P\uparrow$ and $P\downarrow$ states 1T″ $MoS_2$ with lattice vectors of these supercells were oriented along the [210] and [010] directions, respectively. As denoted in Figure 3a, the orthorhombic supercells are marked by blue dashed boxes. For the calculation, three $P\uparrow$ orthorhombic supercells and three $P\downarrow$ orthorhombic supercells are combined. During the structural relaxation process, the regions numbered 5 through 8 and 17 through 20 (Figure 3b) were kept fixed in the middle of both $P\uparrow$ and $P\downarrow$ domains, while other areas were allowed to relax to identify stable DW structures. This process reveals two possible DWs, designated by DW1 and DW2. Using the polarization displacement $\bar{d}_z^S$–$\bar{d}_z^{Mo}$ shown in Figure 3b, we observed that the displacement increases abruptly across the DWs.

Figure 3c,d shows the electronic band structure of the relaxed structure, as illustrated in Figure 3a. Due to the shape of the supercell, the hexagonal Brillouin zone of the primitive cell is folded to the line along the [$\bar{1}$20] direction, perpendicular to transmission (green line in the inset of Figure 3c). In contrast to the bulk band structure shown in Figure 2c, the CBM and VBM in the DW supercell emerge at the Γ point. We project the regions shown in Figure 3a to the band structure and find that the band extrema at the Γ point is majorly contributed by region 12 associated with the DW1 (Figure 3c) and region 24 associated with the DW2 (Figure S4a), indicating that the distortion at the DW significantly influences the local electronic structure. On the other hand, the regions 6 (Figure 3d) and 19 (Figure S4b) at the center of the domains contributed dominantly to the energy local extrema at $\pm K$. The spin splitting above Fermi level at $\pm K$ is 47 meV and 33 meV below Fermi level, indicating that the valleys are well maintained away from the DWs.

**Conductance and ON/OFF Ratio of *n*-VSV.** We then construct an *n*-VSV structure assuming that the transport direction is along the [210] axis of 1T″ $MoS_2$. For the UP states, we directly calculate transmission (and hence conductance) of a homogeneous 1T″ $MoS_2$. Figure 4b shows

Downloaded from pubs.acs.org/ancac3/article-pdf/19/3/3448/42225429/nn4c12812.pdf by WESTLAKE UNIV. Yudi Yang on 17 October 2026


https://doi.org/10.1021/acsnano.4c12812
ACS Nano 2025, 19, 3448−3454

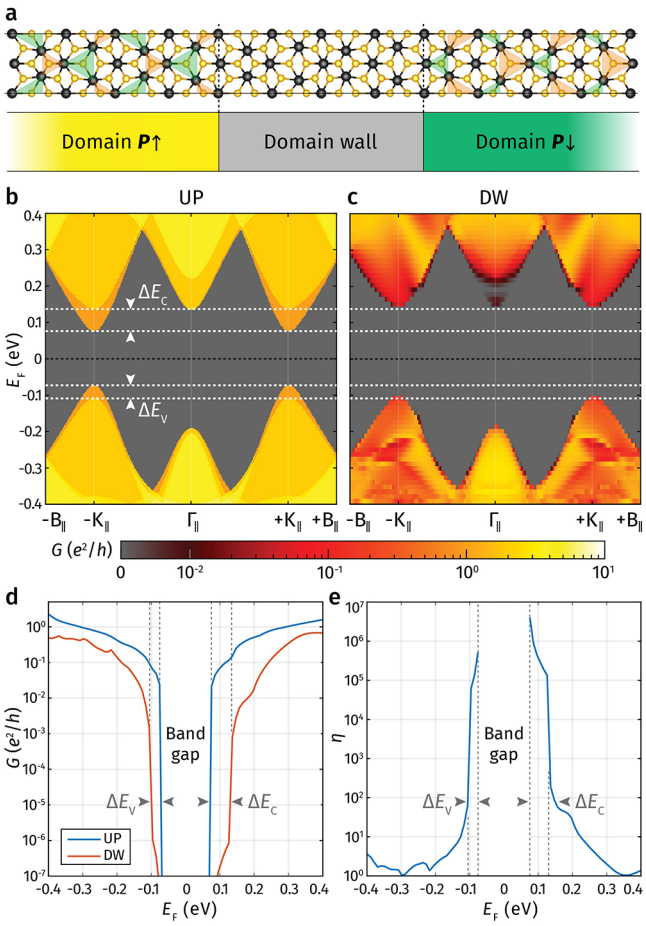


**Figure 4. (a) *n*-VSV structure used for transmission calculations. (b, c) Conductance of the *n*-VSV in the UP state (b) and DW state (c) as functions of the Fermi energy $E_F$ and electron momentum perpendicular to the transmission direction ($k_\parallel$). Conductance is denoted by color, as shown in the color bar in the log scale. (d) Total conductance as a function of $E_F$ for the UP and DW states. (e) ON/OFF ratio as a function of $E_F$.**

conductance $G_{k_\parallel}(E_F)$ as functions of the Fermi energy $E_F$ and transverse wavevector $k_\parallel$ (along $[\bar{1}20]$). Qualitatively, the conductance pattern reflects the band structure, with pronounced valleys at the $\pm K$ points. When $E_F$ lies at the midgap, conductance is zero due to no available electronic states for transport. As $E_F$ enters the valley near CBM, conductance becomes nonzero due to population of the lower spin band. This is evident from the sharp increase in total conductance $G = \sum_{k_\parallel} G_{k_\parallel}$ at this energy (blue line in Figure 4d). The conductance value is $G_{k_\parallel}(E_F) = 1\ e^2/h$ (orange color in Figure 4b) for $E_F$ within $\Delta E_C$, due to only one spin band appearing in the valleys in this energy window. Similar behavior is observed for $E_F$ within $\Delta E_V$.

For the DW states, as shown in Figure 4a, we use 1T″ $MoS_2$ with $P\uparrow$ and $P\downarrow$ domains as the electrodes, and the block of DW1 containing region 5 to region 20 in Figure 3 as the scattering region. We find that the conductance is significantly affected by the presence of DW. $G_{k_\parallel}(E_F)$ is negligibly small at the $\pm K_\parallel$ points for $E_F$ within both $\Delta E_C$ and $\Delta E_V$, as seen from Figure 4c. This suppression of conductance occurs because the valley-dependent spin polarizations in the two domains are opposite. For the $E_F$ far away from CBM and VBM where the valley-dependent spin splitting becomes small, the total conductance $G$ increases sharply as both spin bands get populated (orange line in Figure 4d) enabling scattering between bands with mixed spin polarization.

Figure 4e shows the ON/OFF ratio, $\eta = (G_{UP} - G_{DW})/G_{DW}$, where $G_{UP}$ and $G_{DW}$ are conductances for the UP (ON) and DW (OFF) states, respectively. It is seen that in the energy range of $\Delta E_C$ and $\Delta E_V$, the *n*-VSV exhibits a giant resistive switching effect with $\eta$ being as high as $\sim 10^7$ above the bandgap and $\sim 10^6$ below the bandgap. This huge effect reflects the significant change in conductance between UP and DW states (Figure 4d) due to locking between the spin and electric polarization and represents the key property of an *n*-VSV.

## DISCUSSION

We emphasize that the predicted giant VSV effect is driven by SOC which produces Zeeman-like splitting of the spin bands at non-TRIM momentum valleys. This is, in particular, evident from our calculations without SOC, showing loss of the effect (Figure S7). Therefore, apart from 1T″ $MoS_2$, 2D ferroelectrics with stronger SOC are expected to be beneficial for the design of an *n*-VSV.

The transport properties of an *n*-VSV are expected to depend on the DW width between the two domains with opposite polarizations. We therefore checked the stability of the DW in Figure 3a,b by increasing the size of the supercell in the longitudinal direction and performing structural relaxation, as described in the Supporting Information. Our calculations indicated that the shape and width of DW remained largely unchanged, showing its structural stability. The stability of other possible DWs is discussed in Supporting Information.

As can be seen from Figure 3a,b, DW1 and DW2 have somewhat different atomic structures. We therefore calculated the appearance of the VSV effect for a device with DW2 in the scattering region. Our results indicated qualitatively very similar behavior (Figure S6).

We note that due to the ON/OFF ratio being controlled by the valley-dependent spin matching, it is strongly influenced by the choice of transport direction. For example, the VSV effect is expected to be negligible in a 1T″ $MoS_2$-based VSV if the transport is along the [010] direction. In this case, the valleys at $\pm K$ overlap at the same $k_\parallel$, and hence, momentum-dependent spin polarizations for these valleys cancel out. The ON/OFF ratio in this device is then purely due to the domain wall scattering.

Finally, we emphasize the practical feasibility of the proposed *n*-VSV device. The recent experimental work by Lipatov et al.[34] has demonstrated the solid experimental approach to synthesize the robust T″ phase of $MoS_2$. The synthesized 2D T″ $MoS_2$ layers had an out-of-plane polarization ordering and were stable at ambient conditions. Importantly, polarization was found to be switchable that allowed the formation of the oppositely polarized domains separated by an abrupt domain wall. Practically, *n*-VSV can be implemented using a ferroelectric-field-effect (FET)-like structure, where 1T″ $MoS_2$ serves as an FET conducting channel, whose resistance changes by applying a bias voltage on two gates. The two gates are needed to perform switching between the uniform polarization state and domain wall state: one gate provides a bias to maintain the local polarization pointing to a certain direction, while the other gate allows the local polarization to switch between up- and downstates, thus creating or eliminating the domain wall. The room temper-

Downloaded from pubs.acs.org/ancac3/article-pdf/19/3/3448/42225429/nn4c12812.pdf by WESTLAKE UNIV. Yudi Yang on 17 October 2026


https://doi.org/10.1021/acsnano.4c12812
ACS Nano 2025, 19, 3448−3454

ature performance is guaranteed by a relatively large spin splitting ($\Delta E_C \approx 60$ meV and $\Delta E_V \approx 37$ meV) of the $\pm K$ valleys in 1T″ $MoS_2$. Placing the Fermi level into the $\Delta E_C$ or $\Delta E_V$ regions can be achieved by appropriate doping or by a charge transfer from the substrate or capping layer. These observations lay down a path for the experimental realization of the proposed *n*-VSV concept.

## CONCLUSIONS

Overall, our results demonstrate the viability of using 1T″ $MoS_2$ as the core material for an *n*-VSV. By exploiting the intrinsic ferroelectric properties of this 2D vdW material, we demonstrate nonvolatile control over valley-dependent spin polarization and electron transmission without the need for an external electric field. The resulting nVSV device shows a remarkably high resistance ratio between the ON and OFF states, reaching up to $10^7$, thus validating the concept of nonvolatile valleytronics. This advancement paves a new route for more energy efficient and high-performance valleytronic devices, highlighting the importance of 2D ferroelectrics in future electronic applications.

## METHODS

**Computational Methods.** Our calculations are based on DFT and employ the Vienna ab initio simulation package (VASP)[50] utilizing the projector augmented wave (PAW) method.[51] We use generalized gradient approximation (GGA) with the PBEsol exchange and correlation functional,[52] complying with the calculation settings of ref 34. A plane-wave cutoff energy of 500 eV is used in calculations. For the 1T″ $MoS_2$ monolayer structure calculation, a vacuum layer of 26 Å is added in the out-of-plane direction. The structure is relaxed with an $8 \times 8 \times 1$ Γ-centered *k*-point mesh in the irreducible Brillouin zone. The dipole correction in the *z* direction is included. All of the atomic coordinates are relaxed until the force on each atom is less than 0.001 eV/Å. The validity of the method is checked by calculating the lattice constant of the 1T″ $MoS_2$ monolayer. We find the in-plane lattice constant of 1T″ $MoS_2$ to be 6.34 Å which is close to the values 6.40−6.44 Å reported previously.[34,45] The calculated band structure of the 1T″ $MoS_2$ is consistent with that in ref 32, SOC is included in all band structure calculations.

Transmission is calculated using the nonequilibrium Green's function formalism (DFT + NEGF),[53,54] as implemented with Quantum ATK (Version 2022).[55] The calculations are performed using a device structure which contains three parts: left and right electrodes and the central region which includes the DW (Figure 4a). Left and right electrodes are represented by semi-infinite pristine 1T″ $MoS_2$ orthorhombic supercells. The central area contains the relaxed DW structure and two neighboring pristine 1T″ $MoS_2$ orthorhombic supercells. This extended central area is used to reduce the unintended scattering between the central area and electrodes. The dimension of the central area is $6.34 \times 45.2$ Å, containing 34 Mo atoms and 64 S atoms. The band structure of 1T″ $MoS_2$ is calculated also by Quantum ATK and is confirmed consistent with VASP results. In the transmission calculation, an $8 \times 1$ *k*-point mesh is used for the plane perpendicular to the transmission direction. In the transmission direction, the *k* sampling number is chosen to be 100.

## ASSOCIATED CONTENT

### Supporting Information

The Supporting Information is available free of charge at https://pubs.acs.org/doi/10.1021/acsnano.4c12812.

Nudged elastic band (NEB) calculation of ferroelectric switching of 1T″ $MoS_2$; HSE06 band structure of 1T″ $MoS_2$; domain wall stability; alternative domain-wall structures; transmission across a different domain wall; and transmission without spin−orbit coupling (PDF)

## AUTHOR INFORMATION


### Corresponding Author

**Evgeny Y. Tsymbal** − *Department of Physics and Astronomy & Nebraska Center for Materials and Nanoscience, University of Nebraska, Lincoln, Nebraska 68588-0299, United States;* orcid.org/0000-0002-6728-5480; Email: tsymbal@unl.edu

### Authors

**Kai Huang** − *Department of Physics and Astronomy & Nebraska Center for Materials and Nanoscience, University of Nebraska, Lincoln, Nebraska 68588-0299, United States;* orcid.org/0000-0001-5527-3426

**Kartik Samanta** − *Department of Physics and Astronomy & Nebraska Center for Materials and Nanoscience, University of Nebraska, Lincoln, Nebraska 68588-0299, United States*

**Ding-Fu Shao** − *Key Laboratory of Materials Physics, Institute of Solid-State Physics, HFIPS, Chinese Academy of Sciences, Hefei 230031, China;* orcid.org/0000-0002-2732-4131

Complete contact information is available at: https://pubs.acs.org/10.1021/acsnano.4c12812


### Notes

The authors declare no competing financial interest.

The preprint of this article has been deposited at the condensed matter archive: K.H.; K.S.; D.-F.S.; E.Y.T. Two-dimensional nonvolatile valley spin valve. ArXiv:2408.12028; URL: https://arxiv.org/abs/2408.12028 (August 21, 2024).

## ACKNOWLEDGMENTS

This work was primarily supported by the grant number DE-SC0023140 funded by the U.S. Department of Energy, Office of Science, Basic Energy Sciences (K.H., K.S., E.Y.T.). Calculations based on the NEB method (K.H.) were supported by the National Science Foundation through the EPSCoR RII Track-1 program (NSF Award OIA-2044049). Computations were performed at the University of Nebraska Holland Computing Center.

## REFERENCES


(1) Dieny, B. Giant magnetoresistance in spin-valve multilayers. *J. Magn. Magn. Mater.* **1994**, *136* (3), 335−359.

(2) Moodera, J. S.; Kinder, L. R.; Wong, T. M.; Meservey, R. Large Magnetoresistance at Room Temperature in Ferromagnetic Thin Film Tunnel Junctions. *Phys. Rev. Lett.* **1995**, *74* (16), 3273−3276.

(3) Tsymbal, E. Y.; Pettifor, D. G. Perspectives of giant magnetoresistance. In *Solid State Physics*; Ehrenreich, H.; Spaepen, F., Eds.; Academic Press, 2001; Vol. *56*, pp 113−237.

(4) Yang, H.; Valenzuela, S. O.; Chshiev, M.; Couet, S.; Dieny, B.; Dlubak, B.; Fert, A.; Garello, K.; Jamet, M.; Jeong, D.; Lee, K.; Lee, T.; Martin, M.; Kar, G. S.; Sénéor, P.; Shin, H.; Roche, S. Two-dimensional materials prospects for non-volatile spintronic memories. *Nature* **2022**, *606*, 663−673.

(5) Tsymbal, E. Y.; Mryasov, O. N.; LeClair, P. R. Spin-dependent tunneling in magnetic tunnel junctions. *J. Phys.: Condens. Matter* **2003**, *15*, R109−R142.

(6) Žutić, I.; Fabian, J.; Das Sarma, S. Spintronics: Fundamentals and Applications. *Rev. Mod. Phys.* **2004**, *76*, 323−410.

(7) Tehrani, S.; Slaughter, J. M.; Chen, E.; Durlam, M.; Shi, J.; DeHerren, M. Progress and Outlook for MRAM Technology. *IEEE Trans. Magn.* **1999**, *35* (5), 2814−2819.


Downloaded from pubs.acs.org/ancac3/article-pdf/19/3/3448/42225429/nn4c12812.pdf by WESTLAKE UNIV. Yudi Yang on 17 October 2026

(8) Bhatti, S.; Sbiaa, R.; Hirohata, A.; Ohno, H.; Fukami, S.; Piramanayagam, S. Spintronics based random access memory: a review. *Mater. Today* **2017**, *20* (9), 530−548.
(9) Rycerz, A.; Tworzydło, J.; Beenakker, C. W. J. Valley filter and valley valve in graphene. *Nat. Phys.* **2007**, *3*, 172−175.
(10) Tao, L. L.; Tsymbal, E. Y. Two-dimensional spin-valley locking spin valve. *Phys. Rev. B* **2019**, *100*, No. 161110.
(11) Rehman, M. U.; Kiani, M.; Wang, J. Jacutingaite family: An efficient platform for coexistence of spin valley Hall effects, valley spin-valve realization, and layer spin crossover. *Phys. Rev. B* **2022**, *105*, No. 195439.
(12) Xiao, D.; Liu, G. B.; Feng, W.; Xu, X.; Yao, W. Coupled Spin and Valley Physics in Monolayers of $MoS_2$ and Other Group-VI Dichalcogenides. *Phys. Rev. Lett.* **2012**, *108*, No. 196802.
(13) Schaibley, J. R.; Yu, H.; Clark, G.; Rivera, P.; Ross, J. S.; Seyler, K. L.; Yao, W.; Xu, X. Valleytronics in 2D materials. *Nat. Rev. Mater.* **2016**, *1*, 16055.
(14) Vitale, S. A.; Nezich, D.; Varghese, J. O.; Kim, P.; Gedik, N.; Jarillo-Herrero, P.; Xiao, D.; Rothschild, M. Valleytronics: Opportunities, Challenges, and Paths Forward. *Small* **2018**, *14* (38), No. 1801483.
(15) Zhao, S.; Li, X.; Dong, B.; Wang, H.; Wang, H.; Zhang, Y.; Han, Z.; Zhang, H. Valley manipulation in monolayer transition metal dichalcogenides and their hybrid systems: status and challenges. *Rep. Prog. Phys.* **2021**, *84*, No. 026401.
(16) Xiao, D.; Yao, W.; Niu, Q. Valley-Contrasting Physics in Graphene: Magnetic Moment and Topological Transport. *Phys. Rev. Lett.* **2007**, *99*, No. 236809.
(17) Jiang, Y.; Low, T.; Chang, K.; Katsnelson, M. I.; Guinea, F. Generation of Pure Bulk Valley Current in Graphene. *Phys. Rev. Lett.* **2013**, *110*, No. 046601.
(18) Shimazaki, Y.; Yamamoto, M.; Borzenets, I. V.; Watanabe, K.; Taniguchi, T.; Tarucha, S. Generation and detection of pure valley current by electrically induced Berry curvature in bilayer graphene. *Nat. Phys.* **2015**, *11*, 1032−1036.
(19) Mak, K. F.; McGill, K. L.; Park, J.; McEuen, P. L. The valley Hall effect in $MoS_2$ transistors. *Science* **2014**, *344* (6191), 1489−1492.
(20) Lee, J.; Mak, K. F.; Shan, J. Electrical control of the valley Hall effect in bilayer $MoS_2$ transistors. *Nat. Nanotechnol.* **2016**, *11*, 421−425.
(21) Pan, H.; Li, Z.; Liu, C. C.; Zhu, G.; Qiao, Z.; Yao, Y. Valley-Polarized Quantum Anomalous Hall Effect in Silicene. *Phys. Rev. Lett.* **2014**, *112* (10), No. 106802.
(22) Tao, L. L.; Naeemi, A.; Tsymbal, E. Y. Valley-Spin Logic Gates. *Phys. Rev. Appl.* **2020**, *13* (5), No. 054043.
(23) Tao, L. L.; Tsymbal, E. Y. Perspectives of spin-textured ferroelectrics. *J. Phys. D: Appl. Phys.* **2021**, *54*, 113001.
(24) Cao, T.; Wang, G.; Han, W.; Ye, H.; Zhu, C.; Shi, J.; Niu, Q.; Tan, P.; Wang, E.; Liu, B.; Feng, J. Valley-selective circular dichroism of monolayer molybdenum disulphide. *Nat. Commun.* **2012**, *3* (1), 887.
(25) Sallen, G.; Bouet, L.; Marie, X.; Wang, G.; Zhu, C. R.; Han, W. P.; Lu, Y.; Tan, P. H.; Amand, T.; Liu, B. L.; Urbaszek, B. Robust optical emission polarization in $MoS_2$ monolayers through selective valley excitation. *Phys. Rev. B* **2012**, *86*, No. 081301.
(26) Mak, K. F.; He, K.; Shan, J.; Heinz, T. F. Control of valley polarization in monolayer $MoS_2$ by optical helicity. *Nat. Nanotechnol.* **2012**, *7*, 494−498.
(27) Zhang, X. X.; Lai, Y.; Dohner, E.; Moon, S.; Taniguchi, T.; Watanabe, K.; Smirnov, D.; Heinz, T. F. Zeeman-Induced Valley-Sensitive Photocurrent in Monolayer $MoS_2$. *Phys. Rev. Lett.* **2019**, *122*, No. 127401.
(28) Wang, L.; Xu, Z.; Wang, W.; Bai, X. Atomic Mechanism of Dynamic Electrochemical Lithiation Processes of $MoS_2$ Nanosheets. *J. Am. Chem. Soc.* **2014**, *136* (18), 6693−6697.
(29) Yu, Y.; Nam, G.-H.; He, Q.; Wu, X.-J.; Zhang, K.; Yang, Z.; Chen, J.; Ma, Q.; Zhao, M.; Liu, Z.; Ran, F.-R.; Wang, X.; Li, H.; Huang, X.; Li, B.; Xiong, Q.; Zhang, Q.; Liu, Z.; Gu, L.; Du, Y.; Huang, W.; Zhang, H. High phase-purity 1T'-$MoS_2$- and 1T'-$MoSe_2$-layered crystals. *Nat. Chem.* **2018**, *10* (6), 638−643.
(30) Chou, S. S.; Sai, N.; Lu, P.; Coker, E. N.; Liu, S.; Artyushkova, K.; Luk, T. S.; Kaehr, B. J.; Brinker, C. J. Understanding catalysis in a multiphasic two-dimensional transition metal dichalcogenide. *Nat. Commun.* **2015**, *6*, 8311.
(31) Pal, B.; Singh, A.; G, S.; Mahale, P.; Kumar, A.; Thirupathaiah, S.; Sezen, H.; Amati, M.; Gregoratti, L.; Waghmare, U. V.; Sarma, D. D. Chemically exfoliated $MoS_2$ layers: Spectroscopic evidence for the semiconducting nature of the dominant trigonal metastable phase. *Phys. Rev. B* **2017**, *96*, No. 195426.
(32) Zhuang, H. L.; Johannes, M. D.; Singh, A. K.; Hennig, R. G. Doping-controlled phase transitions in single-layer $MoS_2$. *Phys. Rev. B* **2017**, *96*, No. 165305.
(33) Zhao, W.; Pan, J.; Fang, Y.; Che, X.; Wang, D.; Bu, K.; Huang, F. Metastable $MoS_2$: Crystal Structure, Electronic Band Structure, Synthetic Approach and Intriguing Physical Properties. *Chem.—Eur. J.* **2018**, *24* (60), 15942−15954.
(34) Lipatov, A.; Chaudhary, P.; Guan, Z.; Lu, H.; Li, G.; Crégut, O.; Dorkenoo, K. D.; Proksch, R.; Cherifi-Hertel, S.; Shao, D. F.; Tsymbal, E. Y.; Íñiguez, J.; Sinitskii, A.; Gruverman, A. Direct observation of ferroelectricity in two-dimensional $MoS_2$. *npj 2D Mater. Appl.* **2022**, *6*, 18.
(35) Py, M. A.; Haering, R. R. Structural destabilization induced by lithium intercalation in $MoS_2$ and related compounds. *Can. J. Phys.* **1983**, *61* (1), 76−84.
(36) Wypych, F.; Schöllhorn, R. 1T-$MoS_2$, a new metallic modification of molybdenum disulfide. *Chem. Commun.* **1992**, *19*, 1386−1388.
(37) Jayabal, S.; Wu, J.; Chen, J.; Geng, D.; Meng, X. Metallic 1T-$MoS_2$ nanosheets and their composite materials: Preparation, properties and emerging applications. *Mater. Today Energy* **2018**, *10*, 264−279.
(38) Lei, Z.; Zhan, J.; Tang, L.; Zhang, Y.; Wang, Y. Recent Development of Metallic (1T) Phase of Molybdenum Disulfide for Energy Conversion and Storage. *Adv. Energy Mater.* **2018**, *8* (19), No. 1703482.
(39) Shi, S.; Sun, Z.; Hu, Y. H. Synthesis, stabilization and applications of 2-dimensional 1T metallic $MoS_2$. *J. Mater. Chem.* **2018**, *6*, 23932−23977.
(40) Liu, Y. C.; Wang, V.; Xia, M. G.; Zhang, S. L. First-principles study on structural, thermal, mechanical and dynamic stability of T'-$MoS_2$. *J. Condens. Matter Phys.* **2017**, *29*, No. 095702.
(41) Kan, M.; Wang, J. Y.; Li, X. W.; Zhang, S. H.; Li, Y. W.; Kawazoe, Y.; Sun, Q.; Jena, P. Structures and Phase Transition of a $MoS_2$ Monolayer. *J. Phys. Chem. C* **2014**, *118* (3), 1515−1522.
(42) Wang, H.; Skeldon, P.; Thompson, G.; Wood, G. Synthesis and Characterization of Molybdenum Disulphide Formed from Ammonium Tetrathiomolybdate. *J. Mater. Sci.* **1997**, *32*, 497−502.
(43) Wypych, F.; Weber, T.; Prins, R. Scanning Tunneling Microscopic Investigation of 1T-$MoS_2$. *Chem. Mater.* **1998**, *10* (3), 723−727.
(44) Heising, J.; Kanatzidis, M. G. Exfoliated and Restacked $MoS_2$ and $WS_2$: Ionic or Neutral Species? Encapsulation and Ordering of Hard Electropositive Cations. *J. Am. Chem. Soc.* **1999**, *121* (50), 11720−11732.
(45) Mulhern, P. J. Lithium intercalation in crystalline $Li_xMoS_2$. *Can. J. Phys.* **1989**, *67* (11), 1049−1052.
(46) Yang, D.; Sandoval, S. J.; Divigalpitiya, W. M. R.; Irwin, J. C.; Frindt, R. F. Structure of single-molecular-layer $MoS_2$. *Phys. Rev. B* **1991**, *43* (14), 12053−12056.
(47) Chrissafis, K.; Zamani, M.; Kambas, K.; Stoemenos, J.; Economou, N.; Samaras, I.; Julien, C. Structural studies of $MoS_2$ intercalated by lithium. *Mater. Sci. Eng., B* **1989**, *3* (1−2), 145−151.
(48) Heising, J.; Kanatzidis, M. G. Structure of Restacked $MoS_2$ and $WS_2$ Elucidated by Electron Crystallography. *J. Am. Chem. Soc.* **1999**, *121* (4), 638−643.
(49) Jonsson, H.; Mills, G.; Jacobsen, K. W., Nudged Elastic Band Method for Finding Minimum Energy Paths of Transitions. In

Downloaded from pubs.acs.org/ancac3/article-pdf/19/3/3448/42225429/nn4c12812.pdf by WESTLAKE UNIV. Yudi Yang on 17 October 2026

*Classical and Quantum Dynamics in Condensed Phase Simulations*, Berne, B. J.; Ciccotti, G.; Coker, D. F., Eds.; World Scientific, 1998.
(50) Kresse, G.; Joubert, D. From ultrasoft pseudopotentials to the projector augmented-wave method. *Phys. Rev. B* **1999**, *59*, 1758.
(51) Kresse, G.; Furthmüller, J. Efficient iterative schemes for ab initio total-energy calculations using a plane-wave basis set. *Phys. Rev. B* **1996**, *54*, 11169.
(52) Perdew, J. P.; Ruzsinszky, A.; Csonka, G. I.; Vydrov, O. A.; Scuseria, G. E.; Constantion, L. A.; Zhou, X.; Burke, K. Restoring the Density-Gradient Expansion for Exchange in Solids and Surfaces. *Phys. Rev. Lett.* **2009**, *102*, No. 039902.
(53) Taylor, J.; Guo, H.; Wang, J. Ab initio modeling of quantum transport properties of molecular electronic devices. *Phys. Rev. B* **2001**, *63*, No. 245407.
(54) Brandbyge, M.; Mozos, J. L.; Ordejón, P.; Taylor, J.; Stokbro, K. Density functional method for nonequilibrium electron transport. *Phys. Rev. B* **2002**, *65*, No. 165401.
(55) Smidstrup, S.; Markussen, T.; Vancraeyveld, P.; Wellendorff, J.; Schneider, J.; Gunst, T.; Verstichel, B.; Stradi, D.; Khomyakov, P. A.; Vej-Hansen, U. G.; Lee, M.-E.; Chill, S. T.; Rasmussen, F.; Penazzi, G.; Corsetti, F.; Ojanperä, A.; Jensen, K.; Palsgaard, M. L. N.; Martinez, U.; Blom, A.; Brandbyge, M.; Stokbro, K. QuantumATK: an integrated platform of electronic and atomic-scale modelling tools. *J. Condens. Matter Phys.* **2020**, *32* (1), No. 015901.

Downloaded from pubs.acs.org/ancac3/article-pdf/19/3/3448/42225429/nn4c12812.pdf by WESTLAKE UNIV. Yudi Yang on 17 October 2026



https://doi.org/10.1021/acsnano.4c12812
*ACS Nano* 2025, 19, 3448−3454